The Astrophysical Journal, 690:1264–1271, 2009 January 10 doi:10.1088/0004-637X/690/2/1264

SOLAR CORONAL STRUCTURE AND STRAY LIGHT IN *TRACE*

C. E. DeForest[1], P. C. H. Martens[2], and M. J. Wills-Davey[2]
[1] Southwest Research Institute, 1050 Walnut Street Suite 300, Boulder, CO 80302, USA; deforest@boulder.swri.edu
[2] Smithsonian Astrophysical Observatory, 60 Garden Street, Cambridge, MA 02138, USA
Received 2008 March 19; accepted 2008 August 28; published 2008 December 12

ABSTRACT

Using the 2004 Venus transit of the Sun to constrain a semiempirical point-spread function (PSF) for the *TRACE* EUV solar telescope, we have measured the effect of stray light in that telescope. We find that 43% of 171 Å EUV light that enters *TRACE* is scattered, either through diffraction off the entrance filter grid or through other nonspecular effects. We carry this result forward, via known-PSF deconvolution of *TRACE* images, to identify its effect on analysis of *TRACE* data. Known-PSF deconvolution by this derived PSF greatly reduces the effect of visible haze in the *TRACE* 171 Å images, enhances bright features, and reveals that the smooth background component of the corona is considerably less bright (and hence more rarefied) than might otherwise be supposed. Deconvolution reveals that some prior conclusions about the Sun appear to have been based on stray light in the images. In particular, the diffuse background "quiet corona" becomes consistent with hydrostatic support of the coronal plasma; feature contrast is greatly increased, possibly affecting derived parameters such as the form of the coronal heating function; and essentially all existing differential emission measure studies of small features appear to be affected by contamination from nearby features. We speculate on further implications of stray light for interpretation of EUV images from *TRACE* and similar instruments, and advocate deconvolution as a standard tool for image analysis with future instruments.

Key words: instrumentation: miscellaneous – Sun: corona – Sun: UV radiation

1. INTRODUCTION

All telescopes, including *TRACE* (Handy et al. 1998), scatter light. The principal scattering mechanisms in a space-based telescope include diffraction through the aperture and any obscuration in the beam of the telescope, irregularities or dust on the mirrors themselves, and reflection or scattering in the detector at the focal plane. All these effects contribute to forming broad, shallow wings on the point-spread function (PSF) of the instrument, which describes the image produced by that instrument when viewing an ideal point source of light. These wings are typically 3–5 orders of magnitude fainter than the core of the PSF, but 3–4 orders of magnitude larger, so that a significant fraction of the light incident on the telescope is spread over a large portion of the image.

For discrete scenes such as starfields, broad PSF wings are not greatly important except that they reduce the net efficiency of the telescope by reducing the apparent brightness of point sources. For continuous or near-continuous, high-contrast scenes such as those viewed by solar telescopes, broad scattering wings are quite important: scattering from large distributed bright structures can overwhelm the emission from dark regions in the same image. These effects, while well known, have received little attention from the solar data analysis community when applied to data from normal-incidence EUV telescopes such as *TRACE,* but they are present nonetheless and must be accounted for when interpreting images from *TRACE* (and all other solar telescopes). Not only quantitative analysis, but even some qualitative interpretations of *TRACE* data may be compromised if stray light effects are not accounted for.

X-rays and ultraviolet light are particularly susceptible to scattering and defocus, and efforts have been made to account for PSF effects in previous instruments. For example, Maute & Elwert (1981) attempted blind iterative deconvolution on the X-ray data from *Skylab,* Svestka et al. (1983) applied it to the hard X-ray imaging spectrometer (HXIS) on *SMM*, and Martens et al. (1995) determined a spatially variable PSF for the *Yohkoh*/soft X-ray telescope (SXT) instrument. These studies have largely focused on iterative methods to identify and remove blurring effects caused by a broad PSF core in the subject instruments, though stray light has also been an object of study. Stray light deconvolution was commonly used on SXT data in the latter years of that mission (e.g., Foley et al. 1997; Gburek & Sylwester 2002; Schrijver et al. 2004).

The *TRACE* EUV PSF has been studied by several groups. Lin et al. (2001) used compact, bright flares to study diffraction patterns on the *TRACE* focal plane and concluded that diffraction from the aluminum filter grids used in *TRACE* scatters 19% of incident EUV photons into a highly structured, broad diffraction pattern; they speculated that the scattering may be affecting imaging performance. Gburek et al. (2006) used this scattering pattern both to derive a best-fit PSF core for *TRACE* and also to determine a portion of the emitted EUV spectrum from particular flare events.

In this report, we primarily consider the diffuse scattering wings of the *TRACE* EUV PSF, and particularly their implications for interpreting coronal images. The wings are not readily measured using a point source such as a flare, because the local intensity of the PSF is quite small far from the core. Outside of diffraction maxima the weak scattered signal is overwhelmed by local emission even for bright events such as flares. Deriving the PSF thus requires analysis of occulted images, using an obstructing body such as the Moon or a planet. We examined *TRACE* data collected near the times of several solar eclipses, but did not find a suitable EUV image set that contained a clear image of the lunar limb. On 2004 June 8, Venus passed in front of the Sun, and several 171 Å image sequences were collected as the planet traversed the disk of the Sun and the off-limb corona. We have used those images to derive a semiempirical scattering PSF for the *TRACE* 171 Å channel, and have tested the PSF for correctness by using it to deconvolve several representative images of interesting coronal structures.

In Section 2 we briefly review deconvolution and how it is performed, in Section 3 we describe the forward modeling process and present our measured PSF, and in Section 4 we demonstrate deconvolution of some representative images. Finally, in Section 5 we discuss implications for interpretation of EUV coronal images and recommend deconvolution as a standard reduction pipeline component for future telescopes.

2. REVIEW OF DECONVOLUTION

Compensating for the effect of scatter within a telescope requires *deconvolution*: the telescope convolves the scene with the instrument's PSF; the effects of the PSF can then be removed by postprocessing. Here we briefly review known-PSF deconvolution and how it is performed; the process is much simpler and more robust than "blind deconvolution," which does not require a PSF that is known in advance.

Telescopes in general respond to a point source of light by generating an image that has finite extent. This image is the PSF of the telescope, and generally varies at most slowly across the image plane; in this treatment, we consider it to be constant with respect to the position on the image plane. Images from the telescope are best described as the convolution of the scene being viewed with the PSF of the telescope. The convolution operation spreads out features by integration (summing) over portions of the source scene, weighted by the PSF. For simplicity, we consider only the postsampling image plane and use discrete operations such as summing, rather than smooth operations such as integration.

Convolving an $n_x \times n_y$ pixel image I with a convolution kernel K (the instrument's PSF) involves taking a weighted sum at each location (i, j) in the source image:

$$\left(I \bigotimes K\right)_{i,j} \equiv \sum_{k=-n_x}^{n_y} \sum_{l=-n_y}^{n_y} I_{i-k,j-l} K_{k,l}. \quad (1)$$

By construction, it is clear that convolution is a linear operation, so it can be represented with matrix multiplication of I (treated as an $n_x n_y$-dimensional column vector) by an $n_x n_y \times n_x n_y$ matrix M_K. Undoing the convolution simply requires inverting M_K.

In general, matrix inversion of large matrices is a hard problem (e.g., Claerbout 2004).[3] Fortunately, convolution in real space is equivalent to elementwise multiplication in Fourier space; in other words, the Fourier basis diagonalizes M_K, so that finding its inverse is trivial. This is the well-known *convolution theorem* (a nice treatment and proof may be found in Bracewell (1999)):

$$I \bigotimes K = \mathcal{F}^{-1}(\mathcal{I} \cdot \mathcal{K}), \quad (2)$$

where $\mathcal{F}$ denotes Fourier transformation, the dot product represents elementwise multiplication, and curly vectors $\mathcal{I}$ and $\mathcal{K}$ are the Fourier doubles of their italic counterparts I and K. The Fourier transform $\mathcal{K}$ of the PSF is the *optical transfer function* (OTF) of the telescope, and its magnitude $|\mathcal{K}|$ is the *modulation transfer function* (MTF). Inverting the convolution operation, then, just requires multiplying by the reciprocal of the OTF,

$$I = \mathcal{F}^{-1}(\mathcal{I}) = \mathcal{F}^{-1}\left(\mathcal{I} \cdot \mathcal{K} \cdot \mathfrak{R}(\mathcal{K})\right), \quad (3)$$

where $\mathfrak{R}$ is the elementwise reciprocal operator.

Because Fourier transformation is itself a linear operation, the components inside the Fourier transform in Equation (2) can be pulled out, to write

$$I = (I \otimes K) \otimes K^{\mathrm{inv}}, \quad (4)$$

where $I \otimes K$ is a source image and K^{inv} is the function whose Fourier transform is $\mathfrak{R}(\mathcal{K})$. Equation (4) is useful because it shows that the entire deconvolution operation can be represented as a convolution by a single inverse PSF. If the OTF is known, then K^{inv} is trivial to find. It is just

$$K^{\mathrm{inv}} = \mathcal{F}^{-1}\left(\mathfrak{R}(\mathcal{K})\right). \quad (5)$$

Because of the reciprocal operation, K^{inv} only exists for kernels with no zero Fourier coefficients.

Even when the PSF K is known, deconvolution is not quite as simple in practice as Equation (5) suggests, because of the presence of noise (which is generally a combination of additive uncorrelated noise, multiplicative uncorrelated noise, and calibration error). A typical image can be represented as a (convolved) true focal plane image, plus a noise image (which is not wholly independent of the true image):

$$I = I_{\mathrm{true}} \bigotimes K + N, \quad (6)$$

where N is the noise image. Dividing by $\mathcal{K}$ in the Fourier plane deconvolves the image but also increases the noise term:

$$\begin{aligned} I_{\mathrm{deconv.}} &= \mathcal{F}^{-1}\left(\mathcal{I} \cdot \mathfrak{R}(\mathcal{K})\right) & (7) \\ &= I_{\mathrm{true}} + \mathcal{F}^{-1}\left(\mathcal{N} \cdot \mathfrak{R}(\mathcal{K})\right). & (8) \end{aligned}$$

The noise term is left in Fourier space to emphasize that $\mathfrak{R}(\mathcal{K})$ is a multiplier on the noise level. Most real telescope PSFs attenuate high spatial frequencies; thus, $\mathfrak{R}(\mathcal{K})$ amplifies those frequencies in the noise by the same factor. The amplified noise term at the far right of Equation (8) can easily overwhelm I_{true}.

The theory of *Wiener filters* develops the optimal balance between signal amplification and noise suppression for additive noise for linear filters such as deconvolution (e.g., Press et al. 1989). Rather than develop the ideal Wiener filter for each image, it is convenient to prevent excessive noise amplification with a *normalized reciprocal* that rolls over after a certain level of amplification. We used a simple approximation $\mathfrak{R}_{\alpha,\epsilon}$:

$$\mathfrak{R}_{\alpha,\epsilon}(z) = \left(\frac{z^*}{|z|}\right) \frac{|z|^{\alpha}}{|z|^{\alpha+1} + \epsilon^{\alpha+1}}, \quad (9)$$

where z is complex but α and ϵ are real. $\mathfrak{R}_{\alpha,\epsilon}$ converges to z^{-1} for large values of z and to $z^* \, |z|^{\alpha-1} \, \epsilon^{-\alpha-1}$ for small values of $|z|$ (when compared with ϵ), and rises to a maximum value close to $\alpha\epsilon^{-1}$. Figure 1 demonstrates construction of an inverse kernel using $\mathfrak{R}_{0.5,0.05}$ for the reciprocal.

3. CONSTRAINT OF THE *TRACE* PSF

We generated a PSF using data from the Venus transit of 2004 June 8, assuming that Venus emits no EUV light. The images were prepared, cleaned, and aligned, and a forward model of the scattering was made by convolving the EUV solar images with a PSF to determine the effect of the emission on the center of the Venus image. We generated a forward model PSF that had a narrow core (because we were not interested in sharpening the images, only in reducing stray light) and included a priori

---

[3] Image Estimation by Example, Stanford Exploration Project. http://sepwww.stanford.edu/sep/prof/gee

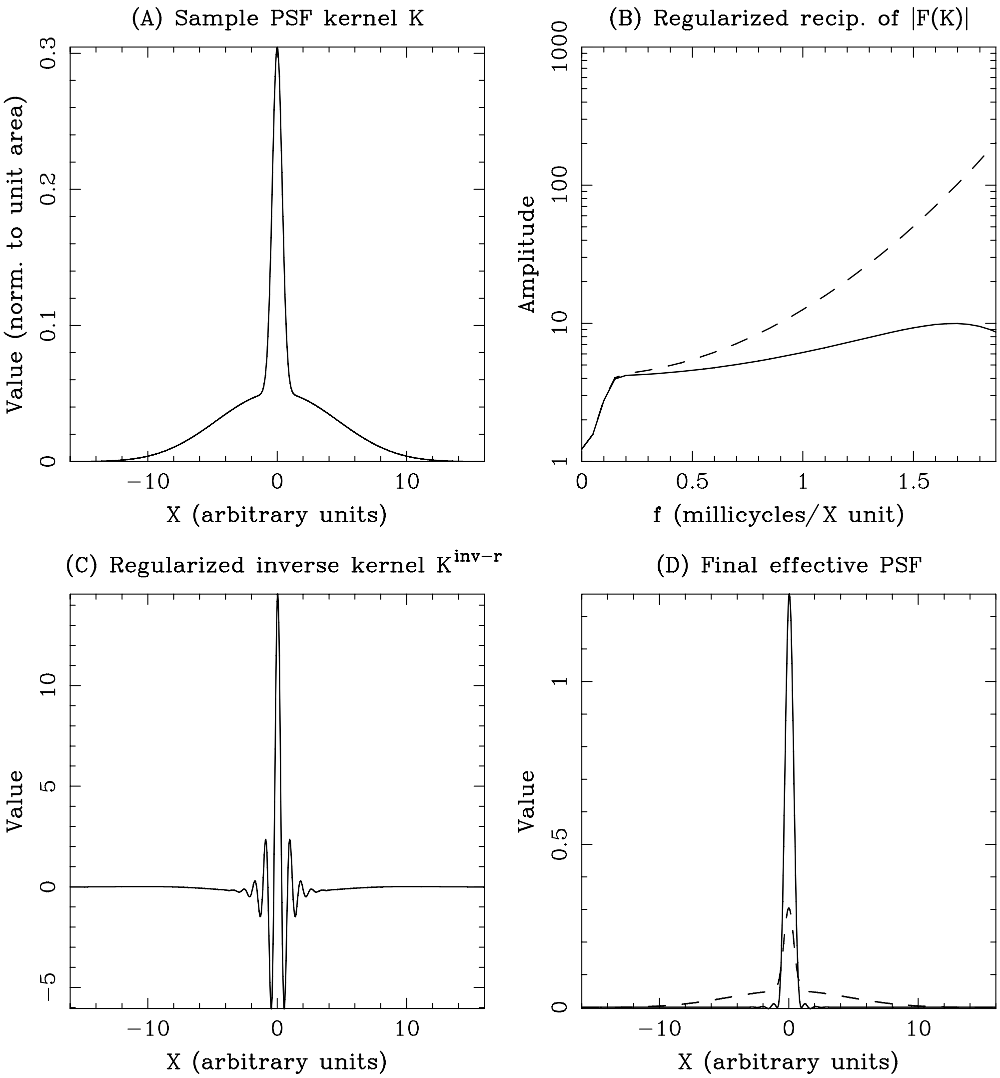

Figure 1. Inversion of a sample circularly symmetric kernel using the Fourier transform and regularized reciprocation. (A) Original sample PSF, K; (B) true (dashed) and regularized (solid) reciprocal of the Fourier components of K; (C) resulting inverse kernel K^{inv}; (D) convolution of $K \bigotimes K^{\mathrm{inv}}$ would be a delta function in the ideal case; it is much improved over the original in (A), which is overplotted as a dashed line.

the known 171 Å diffraction pattern first described by Lin et al. (2001). Added to the core and the diffraction pattern was a broad truncated Lorentzian described by three parameters: the height, the width parameter, and the width of a Gaussian envelope that was used to truncate the Lorentzian. We convolved the parameterized PSF with the solar EUV images (with the portion inside the disk of Venus masked to black) and calculated a model intensity at each of the 12 test loci within the disk of Venus: the center of each of the six images of the planet, and two offset loci in each of the three on-disk images. We compared these model intensities to the original image brightnesses at the test loci, and adjusted the parameters to find the best fit for all the 12 loci.

3.1. Image Preparation

Two sets of *TRACE* EUV images are present from the Venus occultation, both in the 171 Å passband. During the transit itself many images were taken with no binning and either 16 s, 30 s, or 90 s exposure (in the hour 09:00–10:00 UT); and shortly after the transit a series of images with 16 s exposure and 2×2 binning were collected off-limb (in the hour 11:30–12:30 UT). On-disk, we used the 90 s exposures to minimize background noise; off-limb, we median-filtered blocks of five images along the time axis to reduce background noise in those less-well-exposed frames. Figure 2 shows a sample on-disk and off-limb image. We downloaded level 1 data directly from the *TRACE* Web site. We further corrected the zero point by subtracting the average of the 30×30 pixel region in the lower-left corner of each *TRACE* image (in the filter vignetted area), then scaled the images to $1''$ per pixel (thus reducing the on-disk images to match the 2×2-binned off-limb images) and divided out the exposure time and binned pixel size to arrive at photometric images given in ct arcsec^{-2} s^{-1}, so that the images were directly comparable. We despiked each image using a simple unsharp-mask plus threshold algorithm (the “spikejones.pdl” routine in the PDL portion of the *Solarsoft* software distribution (Freeland & Handy 1998), and replaced each spike value with the median) of valid values in its neighborhood in the same image. We made a five-image pixelwise median of the off-limb images, then spatially shifted each image to center Venus in the frame (Figure 3).

Because *TRACE* has a limited field of view, but the primary and secondary mirrors are exposed to the entire solar disk, it

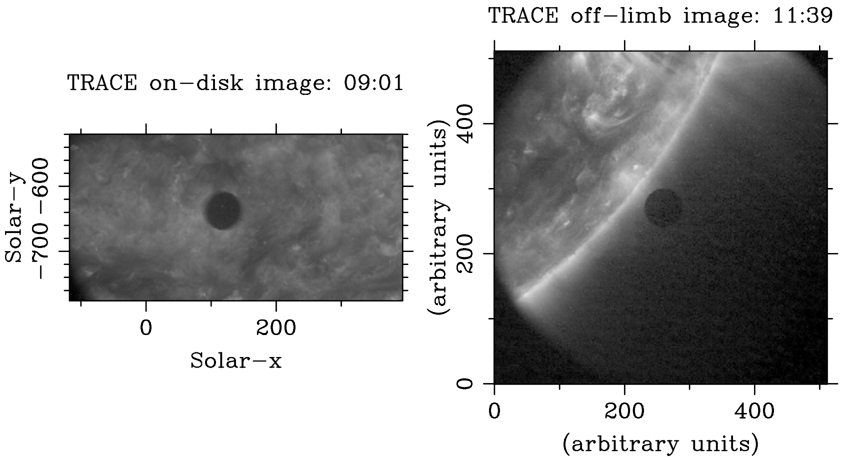

Figure 2. *TRACE* EUV images of the 2004 Venus transit (left) and its immediate aftermath (right), showing the restricted size of the on-disk field of view. The images were extended by combining them with the closest EIT image at the same wavelength.

was necessary to extend the field of view to a good fraction of the solar disk to model the extended PSF and reduce the possibility that edge effects would affect the result. We used the closest-in-time full-disk 171 Å image from *Solar and Heliospheric Observatory* (*SOHO*)/EUV Imaging Telescope (EIT) (Delaboudiniere et al. 1995), collected at approximately 19:00 UT on the same day, to fill in missing values outside the *TRACE* field of view. Although the EIT image was collected some 7–9 hr after the Venus occultation data, the portions of the solar image that are affected are far from the test loci in the disk of Venus, and therefore only large spatial scales are important; brightness on these scales varies on timescales of hours to days. The EIT image was prepared using the instrument-supplied eit_prep software, scaled to 1″ per pixel, derotated to the *TRACE* time, and multiplied so that a 100 × 100 pixel sum (chosen to be far from the *TRACE*-vignetted regions) was equal between the EIT and *TRACE* image. Then the dark (vignetted) portions of the *TRACE* image were replaced with the corresponding portion of the scaled, corrected EIT image. Figure 3 shows all of the resulting cleaned, combined images and the loci within them that were used to constrain the fit.

3.2. *Forward Modeling of the PSF*

We forward modeled the scattering portion of the *TRACE* PSF as the sum of the measured diffraction pattern (Lin et al. 2001; Gburek et al. 2006) and a circularly symmetric scattering profile produced by revolving a radial function about the origin. The revolved function was a sum of a narrow core, a "shoulder" Gaussian, and a truncated Lorentzian intended to represent the scattering wings. The central core width was chosen to have a value much less than the Gburek et al. (2006) width, because the intent is to remove scattering wings rather than to sharpen the core of the PSF by deconvolution. The diffraction pattern was convolved with the central core to avoid pixelization artifacts due to the delta functions in it.

The analytical formula is

$$K_{\alpha,w,\sigma}(r,\theta) = \gamma\left(\left(e^{-4ln(2)r^2}/1.27\right) \otimes D(r,\theta) + \frac{\alpha}{r^2/w^2+1}e^{-4ln(2)r^2/\sigma_t^2} + \beta e^{-4ln(2)r^2/\sigma_s^2}\right), \qquad (10)$$

where r is the distance in the image plane, measured in arcseconds; the 1.27 normalizes the integral under the first Gaussian to unity; $\otimes$ represents convolution; $D(r,\theta)$ is the diffraction pattern described below, including a central core; α is relative strength of the Lorentzian wings; w is the width of the Lorentzian; σ_t is the full width at half-maximum (FWHM) of the truncating Gaussian (in arcsec); β is the strength of a Gaussian shoulder to the curve; σ_s is the width of the shoulder; and γ is a factor to normalize the integral under the two-dimensional convolution kernel to unity.

The parameters were found by an iterative fit method: for each guess set of parameters, the kernel was calculated on an $800'' \times 800''$ grid at $0''\!.5$ resolution, multiplied by each of the six composite images, and summed to find the expected scattered intensity at the center of each Venus image. Note that the *TRACE* field of view is only about 500″ across—the larger field of view (available with the EIT overlay) was used so that the *TRACE* field of view, itself, would not constrain the fits.

In addition, we used an offset kernel to calculate the intensity at an off-center locus in each of the three on-disk images, to constrain the shoulders of the curve a few arcseconds from the core. We did not use the off-center brightness in the off-limb Venus images, because pixels above the limb of the Sun probably contain proportionally more scattered light than do pixels on the solar disk. The geometry of each sample point is shown in Figure 3. We compared the intensities to the forward scattering model and adjusted the parameters initially "by eye" to find a reasonable match with the 12 data points. Finally, we optimized the fit with an amoeba algorithm (e.g., Press et al. 2007), holding $w_{\rm core}$ at the conservative 0.5 arcsec FWHM and penalizing errors in the overcompensation direction (taking the image value below zero) a factor of 100 times worse than errors in the undercompensation direction. The resulting parameters are given by

$$\begin{aligned} \alpha &= 2.06 \times 10^{-5}, \\ w &= 57.7\,\text{arcsec}, \\ \sigma_t &= 68.4\,\text{arcsec}, \\ \beta &= 6 \times 10^{-7}, \\ \sigma_s &= 15\,\text{arcsec}\,. \end{aligned} \qquad (11)$$

The fit is within 0.021 ct arcsec^{-2} s^{-1} of the measured data value at each sample point and 0.019 ct arcsec^{-2} s^{-1} rms across the 12 data points, compared to absolute brightnesses of 0.5–1 ct arcsec^{-2} s^{-1} in the interior of the disk of Venus. The fitted PSF and its inverse are plotted in Figure 4. There is no significant contribution to the total energy outside of a

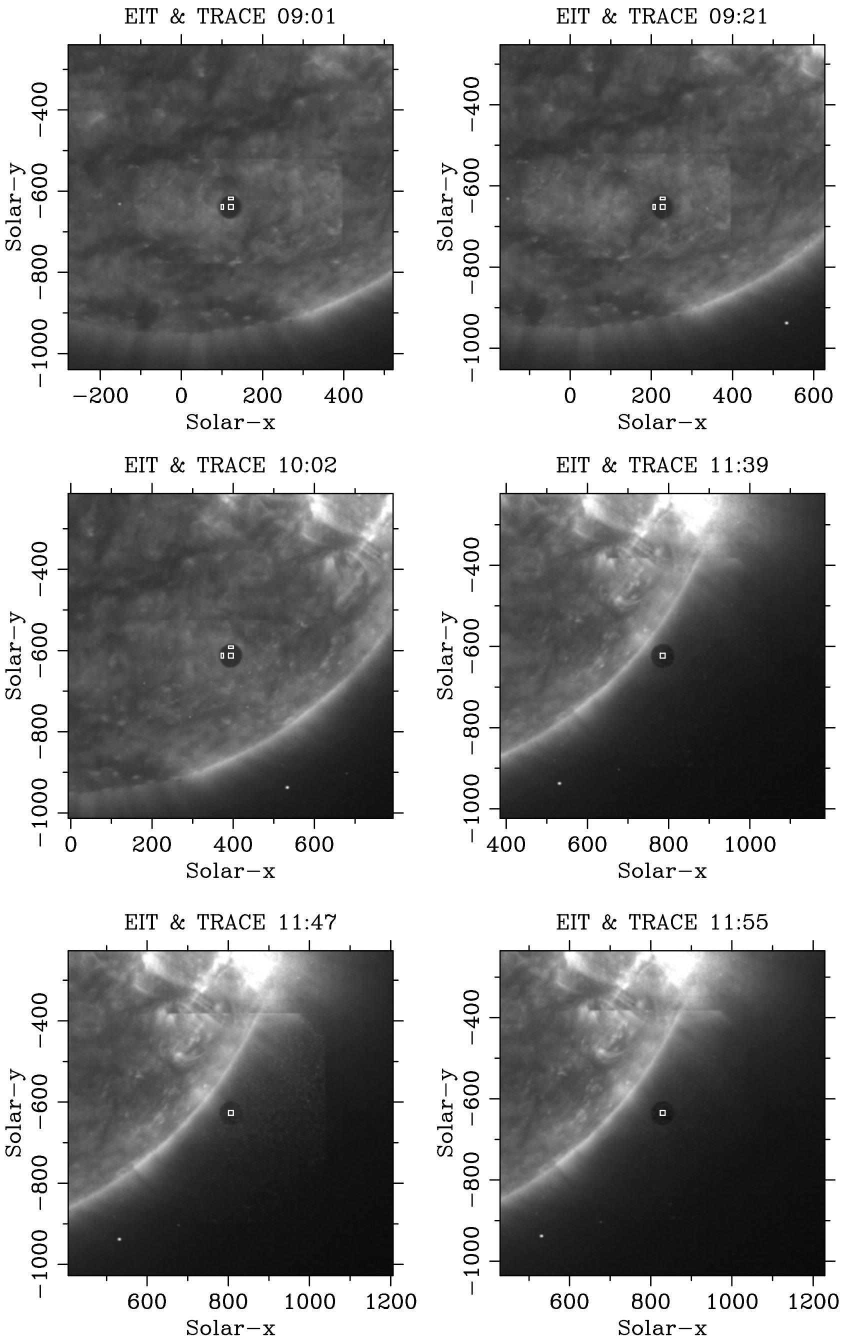
EIT & TRACE 09:01

EIT & TRACE 09:21

EIT & TRACE 10:02

EIT & TRACE 11:39

EIT & TRACE 11:47

EIT & TRACE 11:55

Figure 3. Regularized images from the 2004 June 8 Venus transit used for fitting the *TRACE* scattering PSF. The EIT image from 19:00 UT has been used to fill in the missing regions outside the original field of view. The field of view is 800″ across; the best-fit PSF has a scattering full-width of ∼300″. The sample regions are marked: each image is sampled in a 12″ × 12″ square at the center of the (58″ diameter) disk of Venus, and disk images are also sampled in a 12″ × 6″ rectangle offset 18″ above the center of the disk, and 6″ × 12″ rectangle offset 18″ left of the center of the disk.

100″ radius. The maximum intensity in the PSF core is 0.5; hence, the modeled isotropic scattering function is down by 5 orders of magnitude from the center of the PSF. Nevertheless, its large cover compared to the core of the PSF yields a significant amount of scattering.

The encircled energy is plotted versus distance in Figure 5. The encircled energy curve can be counterintuitive at first: while the scattering wings start and remain small (at under 10^{-3} of the intensity at the core of the PSF), at each successive radius more area is available to contribute to the total integrated energy. Hence, in a nearly uniform scene most of the stray light at a given point in the image plane arises from features 20–50 arcsec (40–100 *TRACE* pixels) away. Approximately 43% of the energy in the derived PSF exists more than 2″ from the center of the core.

4. DECONVOLUTION OF SAMPLE *TRACE* IMAGES

Scattering of 43% has a significant impact on images collected with *TRACE.* Here, we present the results of deconvolution, using the measured PSF from Section 3. A broad variety of 171 Å images were deconvolved and tested for correctness. In no case did any of the pedestal-subtracted, deconvolved images have significant negative-flux regions, an indication that the fitted PSF is either correct or conservative compared to the real

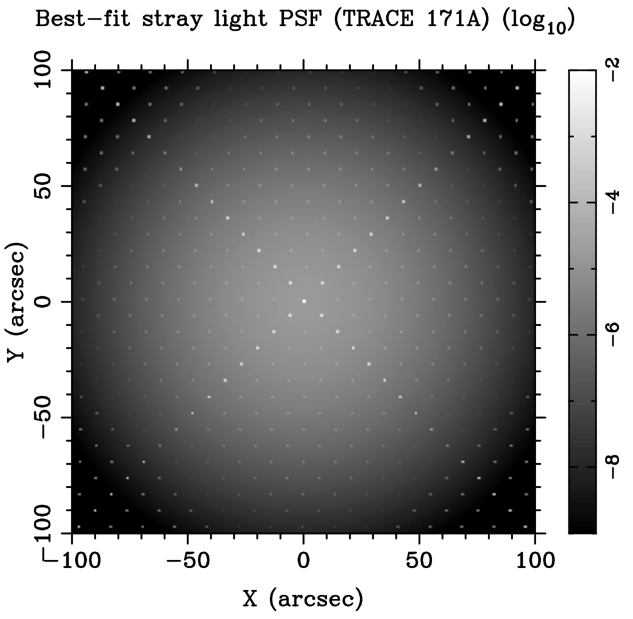

Figure 4. Best-fit PSF (and its inverse) for the 171 Å channel of *TRACE*. The intensity is plotted on a log scale and is normalized to an integral of unity.

PSF of the instrument. Isolated pixels may be carried below zero, due to JPEG artifacts or photon counting noise, but smoothing the image with a 5 × 5 pixel boxcar kernel eliminates the negative regions. In general, bright features get marginally brighter, and dark regions get much darker, after deconvolution. Figure 6 shows the results of deconvolution of a limb scene, a near-disk-center scene, and several dark prominences near the limb. All of the images have been cropped to the middle 500 × 500 pixels of the *TRACE* detector after deconvolution, to avoid edge effects.

The images were despiked using a spatial spike finder ("spikejones.pdl" in the *Solarsoft* distribution; Freeland & Handy (1998)). In each case, the median value of the lower, left 15 × 15 pixel region from each despiked *TRACE* image was used as a zero-point reference: because *TRACE* is vignetted by the thin-foil filter ring on board, the lower-left corner serves as a reasonable dark reference value. No additional background subtraction was performed.

In general, contrast is greatly enhanced throughout the images. For example, the lane in the disk-center active region (center row of Figure 6) is shown to be about a factor of 3 darker than might be expected from naive analysis of the image (without deconvolution), and small features embedded in bright regions (such as the fan of threads on the right-hand side of that image) can be as much as doubled in contrast relative to their local background. The prominences in the bottom row of Figure 6 demonstrate the effectiveness of deconvolution at removing nearby coronal brightness: the prominences (which protrude about one density scale height at 1 MK, hence two intensity scale heights) are shown to be quite dark, presumably because they protrude above most of the quiet coronal emissions. The leftmost prominence is directly behind a loop base and is therefore not darkened nearly as much as the others; this forms a good check that the deconvolution is not simply darkening features arbitrarily. The second-from-left prominence is seen between two bright loop structures, and is hence quite dark despite the apparent bright foreground.

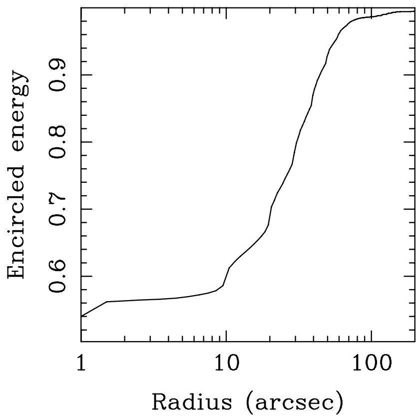

Figure 5. Encircled energy vs. distance for the model PSF calculated with Equations (10) and (11). About 57% of the PSF's total energy is contained in the central core, and 43% is contained in broad scattering wings that extend about 100″ (200 *TRACE* pixels) in all directions. The "wobbles" in the curve are due to successive diffraction maxima.

5. DISCUSSION

The result that *TRACE* images contain a significant amount of scattered light is not, in itself, new. Most telescope PSFs include scattering wings, and *TRACE* is no exception. The filter grid in the front of the telescope is known to scatter ∼20% of incident light into a structured diffraction pattern with myriad local maxima (Lin et al. 2001; Gburek et al. 2006). The present analysis is new in three important respects: it is (to our knowledge) the first analysis of scattered light using *TRACE* occultation data to derive a PSF; much more scattered light is found than can be accounted for merely by diffraction; and the process is taken to its natural conclusion of deconvolving the original *TRACE* images to show the effect of the stray light on scientific interpretation of the images.

The *TRACE* Venus data are not detailed enough to constrain a highly structured PSF model, but the simple empirical fit described here is sufficient to improve existing images via deconvolution, and passes the most basic of deconvolution tests, suggesting that it is not overcompensating for the scattering wings. Deconvolution with our scattering PSF has a similar effect on background subtraction in the interpretation of small features: for features that are small compared to the scattering wings, the effect of the surrounding bright features is approximately constant, so the subtraction of a modeled or fixed background yields similar effects in particular local areas of a given *TRACE* image. The principal advantages of deconvolution are that an approximation of absolute brightness is reproduced, rather than the offset relative brightness that may be extracted from simple background-subtracted images; and that moderate-scale features are treated correctly (they are not treated correctly by simple background or pedestal subtraction).

Deconvolution not only darkens the faintest portions of the image, it also increases the relative contrast of small bright features embedded in a bright background and affects the photometric estimates of the relative density of any small bright feature seen with *TRACE*. This describes several features of interest in the *TRACE* data, including active-region threads that are a subject of current debate (Watko & Klimchuk 2000; Warren & Winebarger 2003; Fuentes et al. 2006; DeForest 2007).

The greater coronal contrast we find in deconvolved *TRACE* images gives indirect support to the idea that the corona is close to hydrostatic equilibrium despite the observed tallness of

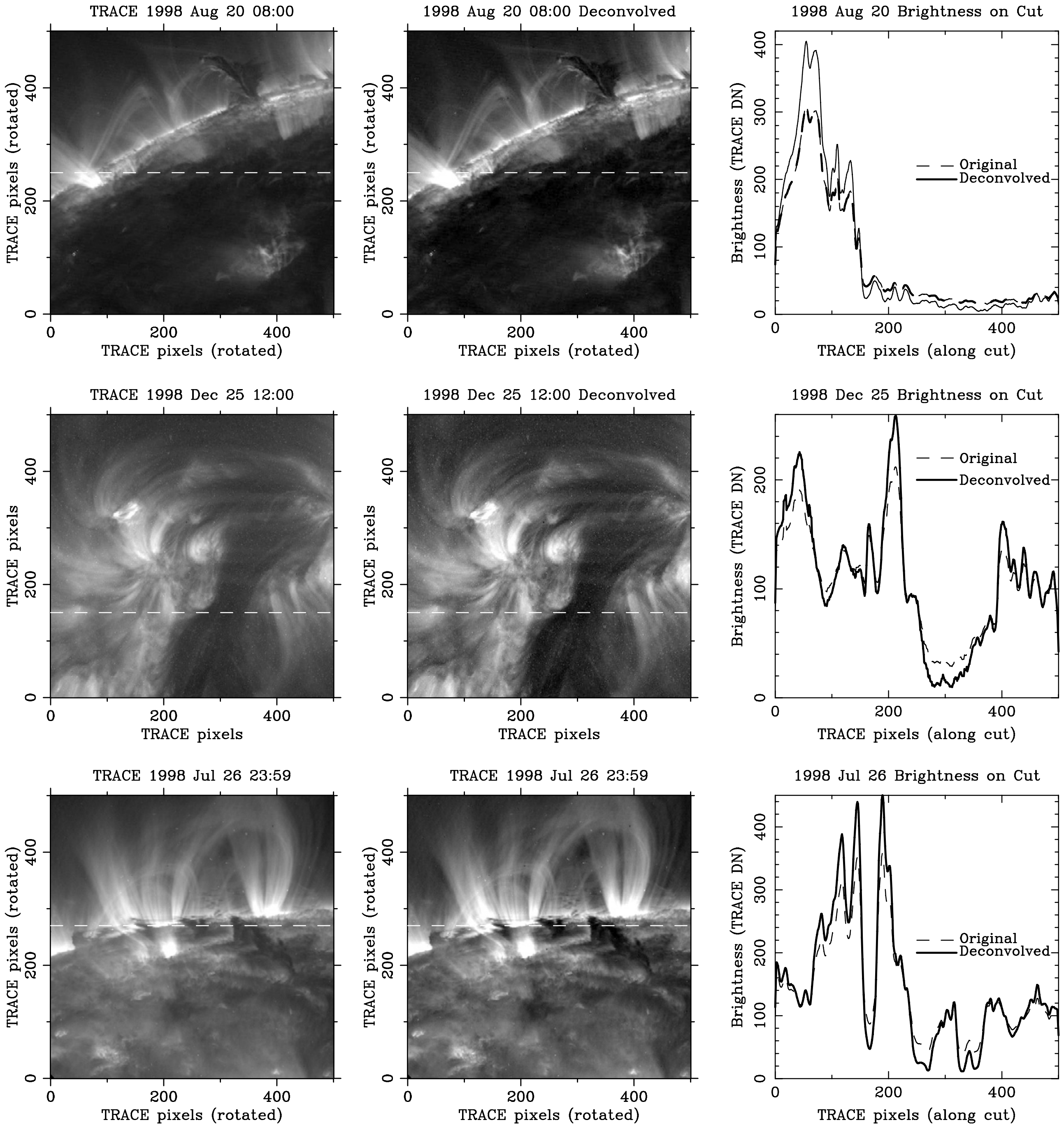

Figure 6. Deconvolution of sample *TRACE* 171 images greatly increases contrast of dark features, eliminates "haze." Top: limb scene. Center: disk AR. Bottom: prominences near the limb. In each row, left is a level-1 processed *TRACE* image; middle is the same image, deconvolved; and right is a plot of brightness along the indicated cut. Compact bright features (such as the small active region at the left-hand side of the top panel) are increased by nearly 50% in brightness; dark features in the midst of bright regions (such as the dark lane near the center of the central image, or the dark prominences at bottom) are darkened by a factor of about 3. Note that the prominence at far left of the lower panel is behind a large bright loop structure, while the others in that image are not.

bright features such as active region loops. The coronal density scale height is about 50 Mm at 1 MK, so the emissivity scale height of Fe IX and Fe X emission line features (close to 1 MK ionization temperature) is about 25 Mm (0.035 R_S) assuming local thermal equilibrium. Thus the EUV-visible corona might be expected to form a thin layer near the photosphere with no significant emission arising at altitudes higher than about 0.07 R_S. Essentially all *TRACE* EUV images show significant background brightness high in the corona; the brightness is visible above the detector "pedestal," because there is contrast between dark but "live" pixels that are part of the image, and corner pixels that are vignetted by the round filter mount at the back of the instrument. The current measured instrument PSF suggests that most or all of this background brightness is due to scattering within the telescope, because dark features (such as the prominences in the bottom row of Figure 6) are reduced nearly to zero brightness when deconvolved. This is the general behavior to be expected from a thin hydrostatic atmosphere at a particular temperature: tall features that are more than 1–2 scale heights tall should have little or no emission above them.

Active region loops appear to have a large scale height compared to that expected for 1–2 MK plasma (Schrijver & McMullen 2000; Aschwanden & Nitta 2000; Winebarger et al. 2003; Fuentes et al. 2006; DeForest 2007). Three explanations that have been advanced are resonant scattering of EUV (which varies as n_e rather than n_e^2), support by nonhydrostatic momentum transport mechanisms such as siphon flows or wave motion, or geometric considerations that attenuate brightness at the bases of the loop. Our result that the quiet corona appears to be consistent with the expected hydrostatic scale height seems to eliminate resonant scattering as a mechanism for tallness, because it would imply a stronger haze in the foreground at high solar altitudes. Further, it seems to limit the functional form of anomalous support mechanisms that could lengthen active region loops' scale height, because such mechanisms must act preferentially on active region loops and not quiet sun loops, to be consistent with the morphology of the deconvolved images. This can be further construed as circumstantial evidence for a geometric, rather than intrinsic, explanation for active region loops' long apparent length (DeForest 2007).

Moore et al. (2008) have recently used image-processing techniques to separate the hazy and sharp components of active region loops viewed with *TRACE*. Such analyses rely on the sharp component of the corona as an indicator of stray light. With 43% scattering of the total light incident on the telescope, 57% is left to be focused; hence, we expect that the hazy portion of such separated image pairs derived from *TRACE* 171 Å data should contain about 75% as much total brightness as the sharp portion does, on the basis of stray light alone.

In addition to morphological differences, corrections to the relative brightness of features such as active region threads and voids affect parameters such as the derived Alfvén speed, because of the n_e^2 dependence of EUV emission. Structures with spiky density profiles emit more EUV per electron than smooth structures do, and the inferred Alfvén speed depends both on the magnetic field and the derived electron density. Onset of some *TRACE*-observed EIT waves appears to require high Alfvén speeds of up to 3 Mm s^{-1} (Wills-Davey et al. 2007); this high speed is difficult to explain in the presence of a diffuse background corona around the source region of the EIT wave. If in fact active regions contain nearly evacuated regions (as in the center panel of Figure 6), then the variation in Alfvén speed is greatly increased and the region-wide average Alfvén speed may be significantly higher than would otherwise be inferred.

As a final example of the impact of stray light in EUV images, coronal heating properties have been derived (Schrijver et al. 2004) by examining the contrast between coronal holes and bright structures, and may be affected by scattering in *SOHO*/EIT and/or *Yohkoh*/SXT. Specifically, if coronal holes are significantly darker, and bright structures are significantly sharper and brighter, than is apparent in raw EUV and X-ray images, then the coronal heating mechanism may not be as distributed as might otherwise be inferred.

The model PSF that we have derived for *TRACE* is somewhat simplified: we have included, a priori, detailed structure that is known from earlier studies (Lin et al. 2001), and parameterized an additional scattering term based on the empirical behavior of stray light on rough mirrors. We have not taken into account possible anisotropy or spatial variability of the scattering, attempted to gain physical understanding of the causes of the PSF, or modeled scattering phenomena that do not fit within the paradigm of a simple PSF. Based on the measurements of the Venus transit in 2004, we have found that roughly 43% of incident energy is scattered by *TRACE*, so that approximately half of the scattered energy may be ascribed to the diffraction pattern found by Lin et al. and approximately half to other mechanisms. Deconvolution greatly improves contrast in *TRACE* images, raising concerns about the interpretation of those images.

More generally, deconvolution to increase contrast in images with scattering wings is strongly recommended for observation from present and future EUV and X-ray telescopes. We have shown that deconvolution can greatly affect the contrast of observed features, and discussed how this may affect a broad variety of science questions. Further, deconvolution to remove broad scattering wings is in general not as hazardous to the data as is deconvolution to increase sharpness in the core of the telescope PSF. This is because there are high spatial frequencies present in the core of the kernel, even if it is added to a much broader distribution, so that noise is not increased as much from deconvolution of a scattering PSF as from a broad PSF core.

Thanks to the *TRACE* and *SOHO*/EIT teams for making their data available to everyone. We also thank L. Golub, J. Cirtain, K. Schrijver, and H. Throop for illuminating discussions, and the anonymous referee for several suggestions that improved the work. *SOHO* is a project of international cooperation between NASA and ESA. This work was funded under NASA's SHP-SR&T program.

REFERENCES

Aschwanden, M. J., & Nitta, N. 2000, ApJ, 535, L59
Bracewell, R. N. 1999, The Fourier Transform and Its Applications (New York: McGraw-Hill)
DeForest, C. E. 2007, ApJ, 661, 532
Delaboudiniere, J.-P., et al. 1995, Sol. Phys., 162, 291
Foley, C. R., Culhane, J. L., & Acton, L. W. 1997, ApJ, 491, 933
Freeland, S. L., & Handy, B. N. 1998, Sol. Phys., 182, 497
Fuentes, M. C. L., Klimchuk, J. A., & Démoulin, P. 2006, ApJ, 639, 459
Gburek, S., & Sylwester, J. 2002, Sol. Phys., 206, 273
Gburek, S., Sylwester, J., & Martens, P. 2006, Sol. Phys., 239, 531
Handy, B. N., Bruner, M. E., Tarbell, T. D., Title, A. M., Wolfson, C. J., Laforge, M. J., & Oliver, J. J. 1998, Sol. Phys., 183, 29
Lin, A. C., Nightingale, R. W., & Tarbell, T. D. 2001, Sol. Phys., 198, 385
Martens, P. C., Acton, L. W., & Lemen, J. R. 1995, Sol. Phys., 157, 141
Maute, K., & Elwert, G. 1981, Sol. Phys., 70, 273
Moore, R. L., Cirtain, J. W., & Falconer, D. A. 2008, Eos Trans. AGU, 89(23), Jt. Assem. Suppl, Abstract SP43C
Press, W. H., Flannery, B. P., Teukolsky, S. A., & Vetterling, W. T. 1989, Numerical Recipes (Cambridge: Cambridge Univ. Press)
Press, W. H., Teukolsky, S. A., Vetterling, W. T., & Flannery, B. P. 2007, Numerical Recipes, The Art of Scientific Computing (3rd ed., Cambridge: Cambridge Univ. Press)
Schrijver, C. J., & McMullen, R. A. 2000, ApJ, 531, 1121
Schrijver, C. J., Sandman, A. W., Aschwanden, M. J., & DeRosa, M. L. 2004, ApJ, 615, 512
Svestka, Z., et al. 1983, Sol. Phys., 85, 313
Warren, H. P., & Winebarger, A. R. 2003, ApJ, 596, L113
Watko, J. A., & Klimchuk, J. A. 2000, Sol. Phys., 193, 77
Wills-Davey, M. J., Sechler, M., & McIntosh, S. W. 2007, AGU Fall Meeting Abstracts, SH31A-0222 (Washington, DC: American Geophysical Union)
Winebarger, A. R., Warren, H. P., & Mariska, J. T. 2003, ApJ, 587, 439